





## Bias dependence and defect analysis of Bi on Si(111) $\sqrt{3} \times \sqrt{3}$ $\beta$ -phase

Longxing Chi <sup>1</sup>, Jun Nogami <sup>1,\*</sup> and Chandra Veer Singh <sup>1,2,†</sup>

<sup>1</sup>Department of Materials Science and Engineering, University of Toronto, 184 College Street, Toronto, Ontario, Canada M5S 3E4

<sup>2</sup>Department of Mechanical and Industrial Engineering, University of Toronto, 5 King's College Road, Toronto, Ontario, Canada M5S 3G8

 (Received 22 November 2020; revised 5 January 2021; accepted 7 January 2021; published 2 February 2021)

We investigate the Bi on Si(111)  $\sqrt{3} \times \sqrt{3}$   $\beta$ -phase surface reconstruction using scanning tunneling microscopy. Details of the bias-dependent images of both the reconstruction and defects are presented. Combining our experimental data with density-functional theory calculations, it is confirmed that the honeycomb pattern at low-bias empty states and hexagonal closest-packed pattern at high-bias empty states originate from the Bi  $p_x$ ,  $p_y$  states and Bi, Si overlapped states outside bulk band gap, respectively. Analysis of the defect images and their associated densities of states provides further insight into the electronic structure of the surface. In particular, we note the presence of a quantum-dotlike localized state associated with an  $\alpha$ -phase defect structure. These results pave the way for further development of surface structures based on Bi on Si(111) surface with unique electronic properties such as sizable spin-orbit coupling, which might be suitable candidates for spintronic applications.

DOI: [10.1103/PhysRevB.103.075405](https://doi.org/10.1103/PhysRevB.103.075405)

### I. INTRODUCTION

Interface science is of great significance in the development of modern integrated electronic devices. Recently, Bi on Si(111) surface reconstructions have been carefully researched due to the extraordinary Rashba-Bychkov (RB) effect that makes them an excellent candidate for spintronics [1–4]. In addition, successful synthesis of 2D bismuthene and the evidence for its quantum spin Hall effect at room temperature has further enhanced the interest in Bi-based interface systems [5].

Initial research regarding the Bi/Si(111) system can trace back to two early studies wherein two phases of the Bi-induced  $\sqrt{3} \times \sqrt{3}$  surface reconstruction, known as the  $\alpha$ - and  $\beta$ -phases, were observed at room temperature using scanning tunneling microscopy (STM) [6,7]. The  $\alpha$ -phase corresponds to a Bi coverage of one-third monolayer (ML) (1 ML =  $7.88 \times 10^{14}$  atoms/cm<sup>2</sup>) with each Bi adatom absorbed on a  $T_4$  site Si [7]. Subsequent low-energy electron diffraction (LEED) and x-ray diffraction (XRD) analysis further confirmed this result [8–10]. In comparison, the  $\beta$ -phase, corresponding to 1 ML Bi coverage, possesses a milkstool structure with every three Bi adatoms constituting a trimer centered at a  $T_4$  site [8,9,11–13]. Furthermore, STM images of the  $\beta$ -phase are highly dependent on sample bias, exhibiting a trimer pattern, honeycomb pattern, and hexagonal-closest-packed (HCP) pattern at filled states, low-bias empty states (LBES), and high-bias empty states (HBES), respectively [1,6,7,14–17]. This bias dependence caused an early controversy whether or not the configuration of  $\beta$ -phase was a trimer or a honeycomb structure. Multiple microscopy techniques as well as density functional theory (DFT) calculations have

corroborated the validity of the former [8,9,11–13,18,19]. However, the detailed origin of the bias dependence of the STM images is still under debate.

In this regard, Nagaoka *et al.* believed that, in empty states, the low-bias honeycomb pattern and high-bias hcp pattern resulted from sublayer Si atoms and adlayer Bi adatoms, respectively, whereas Miwa *et al.* predicted that the previous one originated from Bi surface states while the latter one originated from Si bulk states [12,16]. Furthermore, the bias dependent STM images of identical area of the  $\beta$ -phase have not been presented and understood in the literature thus far, giving rise to less persuasive conclusions on the surface structure and on the bias dependence origin. In this paper, we conduct STM characterization to study the bias dependence for a specified region, using bias-independent defect regions as landmarks, and we provide information about defects that can arise in the  $\beta$ -phase. In combination with our DFT simulations, we confirm the milkstool structure of  $\beta$ -phase as well as its  $T_4$ -site adsorption characteristic. In addition, we clarify details of the origin of the bias dependence in empty states.

### II. EXPERIMENTAL METHODS AND CALCULATION DETAILS

The experiments were performed in an ultrahigh vacuum multifunctional chamber with a base pressure of  $\sim 3.0 \times 10^{10}$  Torr. The clean Si(111)  $7 \times 7$  surface reconstruction was prepared by first degassing the sample overnight at 1100 K followed by few cycles of flashing at 1500 K. Bi adlayers were deposited at room temperature via thermal evaporation at a deposition rate of  $\sim 0.15$  ML/min calibrated by an *in situ* quartz crystal monitor. Bi/Si(111) surface reconstructions were then achieved by postannealing as-deposited sample at  $\sim 630$  K for 10 min. STM was then performed at room temperature. Scanning tunneling spectroscopy (STS) was also conducted

\*jun.nogami@utoronto.ca

†chandraveer.singh@utoronto.ca

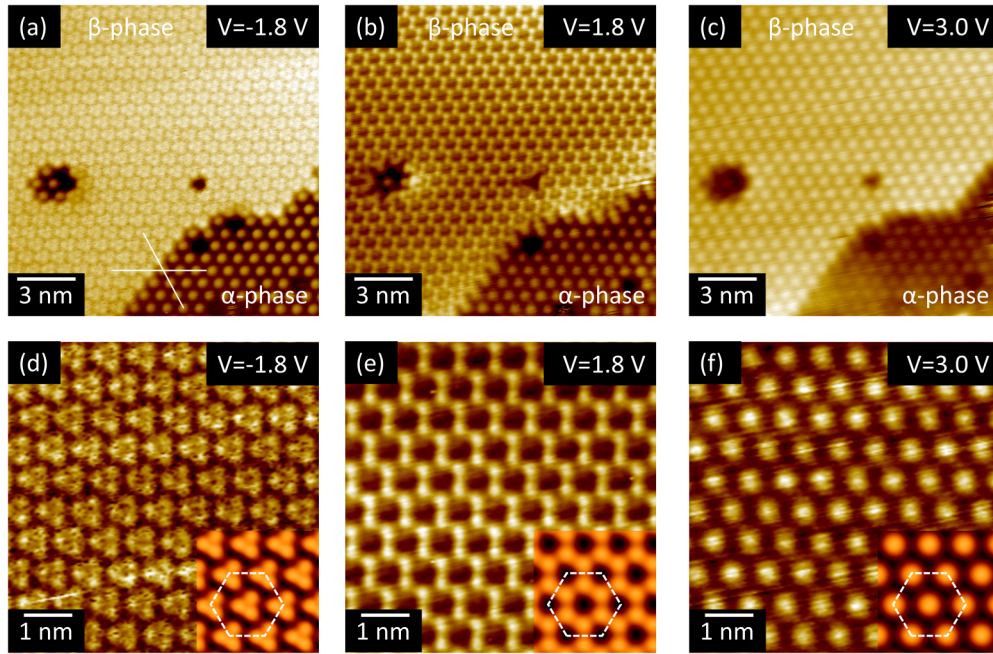


FIG. 1. STM images of Bi on Si(111)  $\sqrt{3} \times \sqrt{3}$   $\beta$ -phase at a sample bias of (a)  $-1.8$  V, (b)  $1.8$  V, and (c)  $3.0$  V, respectively; (d)–(f) zoom-in images of  $\beta$ -phase at same bias as (a)–(c), respectively, where the inset is the DFT simulated STM image.

at a typical feedback setpoints of  $-2$  V (sample bias) and  $0.5$  nA.

DFT calculations were carried out using the Vienna *Ab initio* Simulation Package (VASP) [20]. Generalized gradient approximation with exchange-correlation functional of Perdew-Burke-Ernzerhof in the projector augmented-wave pseudopotentials were implemented [21–23]. The kinetic energy cutoff was set to  $500$  eV. For the purpose of structure optimization, STM simulation, and band-structure calculation,  $5 \times 5 \times 1$  and  $3 \times 3 \times 1$  gamma-centered Monkhorst-Pack grids were used to sample the surface Brillouin zone for the  $\sqrt{3} \times \sqrt{3}$  single unit-cell model and  $3\sqrt{3} \times 3\sqrt{3}$  defect model, respectively; otherwise, a  $10 \times 10 \times 1$  gamma-centered Monkhorst-Pack grid was used for density of states (DOS) calculation [24]. A Si lattice constant of  $3.86$  Å was accepted for our calculations based on our experimental data. In order to correctly simulate the surface, slab models were created consisting of eight Si sublayers and one Bi adlayer plus a  $20$ -Å-thick vacuum space. The bottom layer Si atoms were passivated by hydrogen atoms whose positions were fixed together with the bottom two Si layers during ionic relaxation. The remaining Si and Bi atoms were fully relaxed until the residual force was smaller than  $0.01$  eV/Å and the electron self-consistent threshold was set to be  $10^{-5}$  eV. Spin-orbit coupling was included during all self-consistency calculations. STM simulations were conducted using an algorithm based on the Tersoff-Hamann method [25].

### III. RESULTS AND DISCUSSION

STM images of Bi on Si(111)  $\sqrt{3} \times \sqrt{3}$   $\beta$ -phase at different sample biases are shown in Fig. 1, where Figs. 1(a)–1(c) correspond to a sample bias of  $-1.8$  V (filled state),  $1.8$  V (LBES), and  $3.0$  V (HBES), respectively. All three images represent the same scanning area, which can be easily

confirmed by three distinct landmarks: (1) the bottom-right  $\alpha$ -phase region whose appearance is bias independent, (2) the single trimer-sized  $\beta$ -phase vacancy above the  $\alpha$ -phase defect region, and (3) a flowerlike defect region consisting of five  $\alpha$ -phase defects plus two  $\beta$ -phase vacancies on the left side of the images. The rest of the images are covered by  $\beta$ -phase. Figure 1(a) is a filled-state image in which  $\beta$ -phase exhibits a trimer pattern within a  $\sqrt{3} \times \sqrt{3}$  unit cell, in agreement with previous reports [1,6,7]. At LBES [Fig. 1(b)], the  $\beta$ -phase shows a honeycomb structure, which also agrees with many previous reports [1,6,7,14–17,26]. At HBES [Fig. 1(c)] an  $\alpha$ -phase-like HCP pattern shows up. The threshold bias for the change from the honeycomb pattern to hcp pattern is  $1.9$  V, consistent with that reported by Nagaoka *et al.* [16]. Furthermore, we can easily tell from Fig. 1(a) that  $\alpha$ -phase and  $\beta$ -phase align with each other along two lattice vector directions as labeled by two white lines, showing that the Bi trimers lie on the same site as the single Bi adatoms of the  $\alpha$ -phase, i.e., over the  $T_4$  site.

Magnified images of  $\beta$ -phase at each sample bias are shown in Figs. 1(d) and 1(e). Again, all three images correspond to the same area. The registration of the trimer pattern at filled states [Fig. 1(d)] and the honeycomb pattern at LBES [Fig. 1(e)] is such that they exhibit a phase reversal, i.e., the bright trimer center in empty states is in the same position as the dark hollow in the center of the honeycomb in empty states. Three hexagons in Figs. 1(d) and 1(e) are placed in equivalent positions with apexes over the positions of Bi trimers so that the phase reversal in the STM images can be easily recognized. Based on the milkstool model, the trimer pattern (onsite) reveals the real atomic position whereas the honeycomb pattern (offsite) corresponds to atom-free areas. This bias dependence led to the early confusion about the structure of this surface. To confirm this, DFT calculations were conducted based on the two structures and it turns out

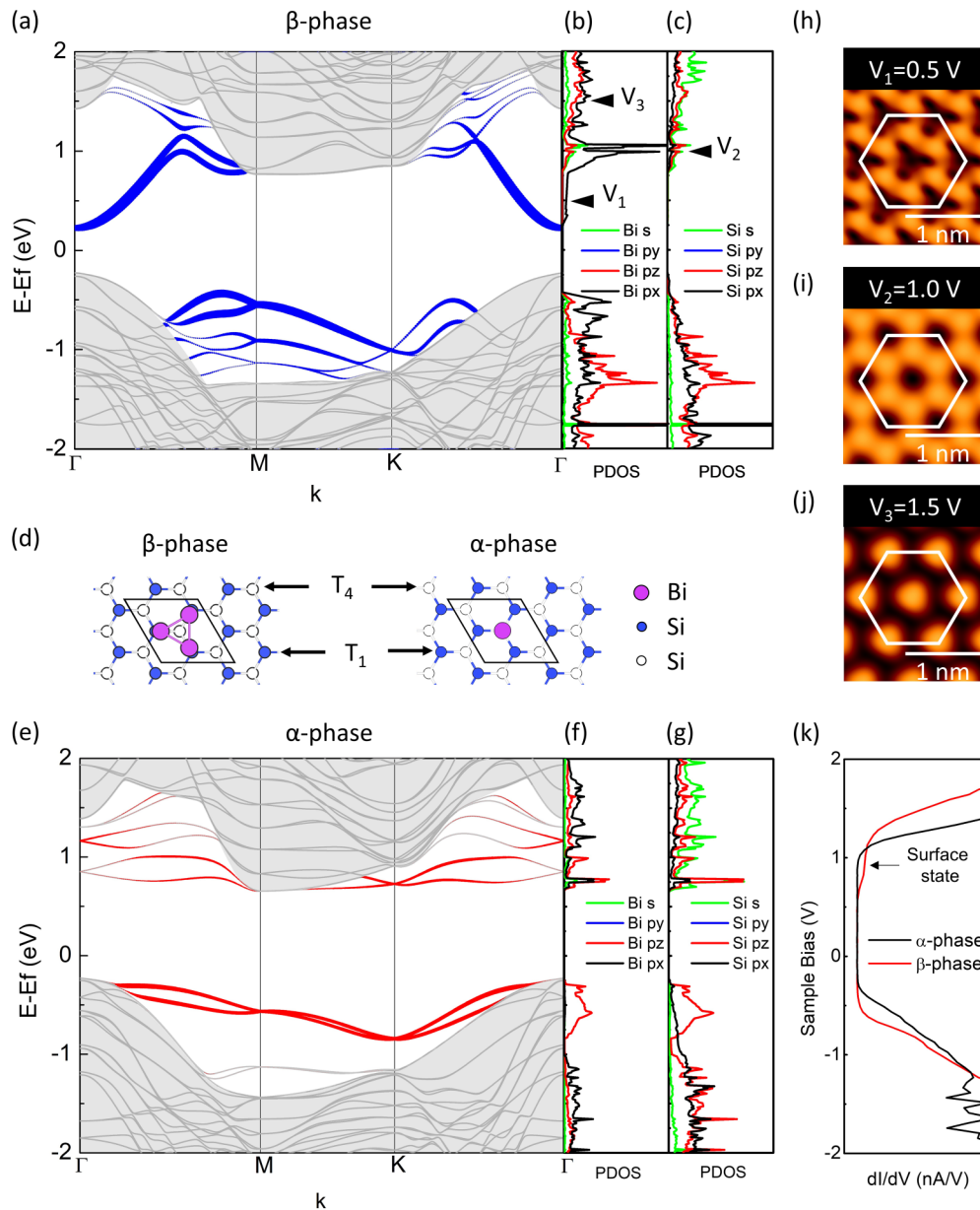


FIG. 2. Band structure and DOS analysis using DFT. (a)–(c) corresponds to  $\beta$ -phase band structure, PDOS of Bi, and PDOS of surface Si, respectively; (d) structural model of  $\beta$ -phase and  $\alpha$ -phase; (e)–(g) correspond to  $\alpha$ -phase band structure, PDOS of Bi, and PDOS of surface Si, respectively; (h)–(j) simulated empty-state STM images at a sample bias of (d) 0.5 V, (e) 1.0 V, and (f) 1.5 V, respectively, where each bias is also labeled in PDOS by black arrow; (k)  $dI/dV$  spectra of  $\alpha$ -phase and  $\beta$ -phase Bi.

that the milkstool model closely reproduces the bias dependence of the STM images. The DFT-simulated STM images for the trimer structure at each sample bias are shown in the insets on the lower right corners of Figs. 1(d)–1(f), and they agree with the experimental images. This result is consistent with previous XRD and LEED studies as well [8,9,11,13].

In order to fully understand the bias dependence of the  $\beta$ -phase in empty states, DFT calculated band structure and projected density of states (PDOS) are shown in Fig. 2. Figs. 2(a) and 2(e) are the band structures of  $\beta$ - and  $\alpha$ -phase, respectively. Si bulk states are represented by light-gray background in both images. Both images show a very similar bulk state outline with a valence-band maximum at  $\Gamma$  point and a conduction-band minimum at  $M$  point, leading to an

indirect band gap. As-calculated bulk-state band gaps for  $\beta$ - and  $\alpha$ -phase are 1.0 and 0.9 eV, respectively, indicating a trivial change in Si bulk-state band structure introduced by two types of Bi surface reconstructions. The Bi states closest to the Fermi energy ( $E_F$ ) are labeled by blue and red solid lines outside the bulk band structure for  $\beta$ - and  $\alpha$ -phase, respectively. The line thickness represents the proportion of corresponding Bi states, which are  $p_x$ ,  $p_y$  states in  $\beta$ -phase [Fig. 2(a)] and  $p_z$  state in  $\alpha$ -phase [Fig. 2(e)], respectively. The most significant difference between the two band structures is that in  $\beta$ -phase there are Bi surface states within the bulk band gap above  $E_F$  and it is those surface states that contribute to the LBES honeycomb pattern. This result is also consistent with Miwa's DFT prediction [12]. Also, our  $\beta$ -phase band



structure is in good agreement with that of previous reports where four bands with prominent RB splitting can be easily observed [2,27].

To better understand why such a difference occurs, PDOS of Bi atoms and surface Si atoms for each phase are calculated and plotted in Figs. 2(b) and 2(c) and Figs. 2(f) and 2(g), with Figs. 2(b) and 2(c) corresponding to  $\beta$ -phase and Figs. 2(f) and 2(g) corresponding to  $\alpha$ -phase. Figure 2(d) shows the atomic structure of both phases, where the largest circles are Bi atoms, and the shaded and white circles show the upper and the lower Si atoms in the underlying bilayer. The adatom adsorption positions over the upper and lower Si atoms are commonly denoted as  $T_1$  and  $T_4$  sites, respectively.

First, in  $\beta$ -phase, overlapping between Bi  $p_z$  orbitals and Si  $p_z$  orbitals, both represented by red lines in Figs. 2(b) and 2(c), can be found within an energy range of  $-1$  to  $-2$  eV suggesting a  $\sigma$ -bond formed between Bi  $p_z$  and Si  $p_z$  orbitals. Similarly, overlapping between Bi  $p_x$  (black line) and  $p_y$  (blue line) peaks can be easily recognized within a low-energy range of  $-1$  to  $1$  eV, indicating those two orbitals are bonded by  $\sigma$ -bonds as well. It must be emphasized here that  $p_x, p_y$  curves overlap with each, therefore only the  $p_x$  orbital shows up in the diagram. In comparison, part of the Bi–Bi  $\sigma$ -bonds locate within Si bulk band gap, which we believe results in the bias dependence of  $\beta$ -phase. The bonding configuration can be better explained by the structural model shown in Fig. 2(d). In the trimer model, each Bi adatom (pink) has one nearest  $T_1$ -site Si neighbor (blue). Since there are five valence electrons ( $6s^2 6p^3$ ) for Bi and two of the  $s$ -orbital electrons already pair with each other, three  $\sigma$ -bonds will be generated among Bi  $p_x, p_y$  orbitals (two Bi–Bi bonds) and between Bi and the underlying  $T_1$ -site Si  $p_z$  orbital (one Bi–Si bond). STM simulation using DFT is then performed at three different biases labeled as  $V_1, V_2$ , and  $V_3$  in Figs. 2(b) and 2(c). Simulated images are shown in Figs. 2(h)–2(j). These simulated images are generated by integrating the DOS from the Fermi level to the respective bias voltages.  $V_1$  is set to be  $0.5$  V that corresponds to Bi  $p_x, p_y$  states only.  $V_2$  is set to be  $1.0$  V such that overlapping between Bi surface states and Si bulk states shows up but the Bi surface states, especially  $p_x, p_y$  states, still play a leading role.  $V_3$  is  $1.5$  V at which the prominent Bi  $p_x, p_y$  peak disappears and Si bulk states become comparable with Bi surface states. The simulated images thus reproduce the phase-reversal process from LBES to HBES. A white hexagon is labeled in all three images at the same position so that the transition can be easily recognized. At  $V_1$  and  $V_2$  where Bi  $p_x, p_y$  states dominate, an off-site honeycomb pattern appears. At  $V_3$  when Si bulk states are nontrivial, an onsite hcp pattern arises. Therefore, we can conclude that the LBES honeycomb pattern results from Bi surface states, especially  $p_x, p_y$  states, while the HBES hcp pattern originates from an accumulated effect between Bi surface states and Si bulk states. Such a phase reversal also indicates that Bi surface states and Si bulk states are localized at different spots: Si bulk states appear right above the Bi trimer (onsite) while Bi surface states locate at atom-free  $T_4$  sites (offsite). It is worth emphasizing that the threshold sample bias for this transition is  $1.0$  V in our DFT calculation whereas it is  $1.9$  V in real experiments due to the intrinsic underestimation of band gaps typical of DFT [28]. The honeycomb pattern at  $V_2$  also

suggests there is a competition between Bi surface states and Si bulk states. According to our defect analysis in the next section, when more than two nearest trimers contribute to an atom-free  $T_4$  site, Bi  $p_x, p_y$  states prevail and offsite patterns are generated, otherwise the overlapped states between Si and Bi take over, leading to onsite patterns.

Second, for the  $\alpha$ -phase, PDOS, depicted in Figs. 2(f) and 2(g), an excellent match can be easily observed between Bi  $p_x, p_y, p_z$  orbitals and Si  $p_z$  orbitals through the whole selected energy range, suggesting stable bonds formed between Bi and Si  $p$  orbitals and no additional surface states occur within the bulk band gap. This phenomenon explains why STM images of the  $\alpha$ -phase are not bias dependent. Bond characteristics, in this case, can also be understood by looking at the  $T_4$ -site adsorption structure model in Fig. 2(d). For each  $\alpha$ -phase Bi adatom there are three nearest  $T_1$ -site Si neighbors, each of which contains a  $p_z$  dangling bond waiting to be saturated. Therefore, Bi  $p_x, p_y, p_z$  orbitals form  $\sigma$ -bonds with each  $T_1$  site Si  $p_z$  orbitals by  $sp^3$  hybridization. Finally, in filled states, no surface states show up within the bulk band gap for both  $\beta$  and  $\alpha$ -phase; therefore, both filled-state images are bias independent.

The Bi PDOS can be experimentally confirmed by STS  $dI/dV$  spectra shown in Fig. 2(k). The black and red curves correspond to the  $\alpha$ - and  $\beta$ -phases, respectively, and a shoulder appears at a sample bias of around  $0.7$  eV (empty states) for  $\beta$ -phase, which can be attributed to the Bi  $p_x, p_y$  states. In our DFT calculated PDOS [Fig. 2(b)] a similar shoulder resulting from Bi  $p_x, p_y$  states shows up at around  $0.2$  eV above the Fermi level, which is consistent with our data. The error in shoulder energy between DFT calculation and STS spectra can be ascribed to the intrinsic underestimation of band gap of DFT as well as to the tip-induced band-bending effect in STS characterization [28,29]. At filled state, the  $\beta$ -phase  $dI/dV$  curve sharply increases at  $-0.6$  V while for  $\alpha$ -phase it increases at  $-0.3$  V. Such a difference also matches our DFT simulation. By comparing Figs. 2(b) and 2(f) it can be seen that Bi  $p_x, p_y$  states in  $\beta$ -phase (closest to the Fermi level) are about  $0.3$  eV lower than the Si bulk states, while the Bi  $p_z$  state in  $\alpha$ -phase (closest to Fermi level) has the same energy as Si bulk states. Also, our STS spectrum for  $\beta$ -phase matches with that in Refs. [17,27] except that band-gap positions may shift to some extent, which can be explained by the tip-induced band-bending effect in STS characterization or by differences in substrate doping [29].

We can also study the bias dependence of surface defects based on our STM images together with DFT simulation. STM images of a single  $\beta$ -phase trimer within an  $\alpha$ -phase domain are shown in Figs. 3(a) and 3(b) with a sample bias of  $-1.8$  V (filled state) and  $1.8$  V (LBES), respectively. A white hexagon centered at the single  $\beta$ -phase defect is drawn in both images whose edge length equals to the Bi  $\sqrt{3} \times \sqrt{3}$  lattice constant, from which we can clearly see that the  $\beta$ -phase aligns with the  $\alpha$ -phase in both lattice vector directions, consistent with the fact that both the  $\beta$ -phase Bi trimer and  $\alpha$ -phase Bi adatoms are adsorbed on the  $T_4$  site. The height profiles of the horizontal dotted line in Fig. 3(a) and 3(b) are shown in Fig. 3(e) where the red and black curves correspond to filled state and LBES, respectively. The relative height difference between  $\alpha$ - and  $\beta$ -phase is  $0.2$  and  $0.22$  Å for filled

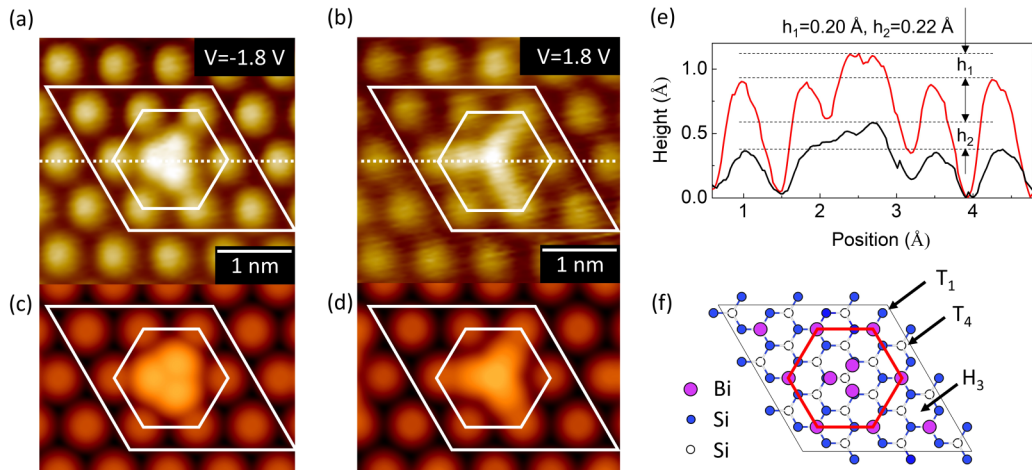


FIG. 3. STM images of a single Bi on Si(111)  $\sqrt{3} \times \sqrt{3}$   $\beta$ -phase defect within an  $\alpha$ -phase domain at a sample bias of (a)  $-1.8$  V and (b)  $1.8$  V, respectively; (c), (d) DFT simulated STM images at filled state and LBES, respectively; (e) height profile of the white dot lines in (a) and (b); the red and black curves correspond to filled and empty states, respectively; (f) unit cell of single  $\beta$ -phase defect model used for DFT calculation, which corresponds to the structure within the (a) white rhombus shown in (a)–(d).

and empty states, respectively. In both cases  $\beta$ -phase is higher than the  $\alpha$ -phase by around  $0.2$  Å.

DFT calculation is performed based on this single  $\beta$ -phase defect model. The supercell used for our DFT simulation is shown in Fig. 3(f) and is also labeled by the white rhombus in Figs. 3(a) and 3(b). The purple, blue, and white circles in the structural model represent Bi, top-layer Si ( $T_1$  site), and bottom-layer Si ( $T_4$  site), respectively. Both  $\alpha$  and  $\beta$ -phase Bi adatoms are placed at  $T_4$  sites. The filled and empty state simulated images are shown in Figs. 3(c) and 3(d), respectively, on the same lateral scale as their experimental counterparts. Excellent consistency can be found between our simulations and experimental results at both biases, suggesting the validity of our  $T_4$ -adsorption model. The fully relaxed defect model exhibits a geometric step increase of  $0.7$  Å in going from the  $\alpha$ -phase to the  $\beta$ -phase. The measured geometric height difference between the two phases is affected by the difference in electronic structure between them. The measured height difference for the images in Figs. 1(a)–1(c) are  $0.3$ ,  $0.3$ , and  $0.6$  Å, respectively; the  $\beta$ -phase is always higher than the  $\alpha$ -phase as is apparent in the images themselves. The measured step-height difference between extended areas of the two phases agree with the measured height of the single trimer defect within experimental error.

It is worth mentioning that the single  $\beta$ -phase defect at LBES in Fig. 3(b), as well as our DFT simulation in Fig. 3(d), exhibits an onsite forked-road pattern rather than an offsite honeycomb pattern shown in Fig. 1(e); also, the above-mentioned phase reversal from filled state to LBES of Bi trimer disappears. Those facts suggest that different states, other than Bi  $p_x$  and  $p_y$  orbitals that contribute to the honeycomb pattern, are playing a leading role. Based on previous band structure and PDOS analysis we believe that the onsite forked-road pattern originates from overlapped Bi and Si states. Besides, disappearance of honeycomb pattern also suggests each honeycomb ring has contributions from more than one Bi trimer.

In order to better illustrate the nature of the Bi  $p_x, p_y$  surface states, STM images of a  $\beta$ -phase vacancy is shown in Fig. 4, where Figs. 4(a) and 4(b) correspond to a sample bias of  $-1.8$  V (filled state) and  $1.8$  V (LBES), respectively. From the filled-state image, we can easily recognize the center vacancy surrounded by  $\beta$ -phase trimers. At LBES, the vacancy transforms into a squeezed triangular shape and the honeycomb pattern integrity is broken due to the existence of the vacancy. Again, we duplicate the vacancy model via DFT and simulated STM images are shown in Figs. 4(c) and 4(d) with the corresponding sample biases. The unit cell used for simulation is shown in Fig. 4(e) as well as labeled in Figs. 4(a)–4(d) by a white rhombus. The simulated images match with our experimental results, suggesting the correctness of the structural model once again.

To understand how the vacancy influences the honeycomb pattern, two red triangles in Fig. 4(e) are highlighted with all their corners and centers sitting at  $T_4$  sites. The difference between the two triangles is that, for the bottom-right triangle, each corner terminates at a Bi trimer, thus the center is surrounded by three nearest trimers. In contrast, for the top-left triangle, two of its corners terminate at Bi trimers while the third corner corresponds to the vacancy. In this case, the triangular center has two nearest trimers only. Same triangles are also labeled in Figs. 4(a)–4(d) for comparison. In Figs. 4(b) and 4(d), the center of the bottom-right triangle exhibits a bright circle that is one-sixth of a honeycomb ring, suggesting intensive energy states are localized at the center. It can be easily realized that three nearest trimers at each triangular corner simultaneously contribute to those localized states at triangular center. Based on what has been discussed above, those states correspond to Bi in-plane  $p_x, p_y$  orbitals. In comparison, the center of the top-left triangle fails to form the same bright circle and adjacent honeycomb integrity is broken. However, it can be discovered that the triangular center is still brighter than the honeycomb center, indicating a small amount of states still exist at the triangular center. It is

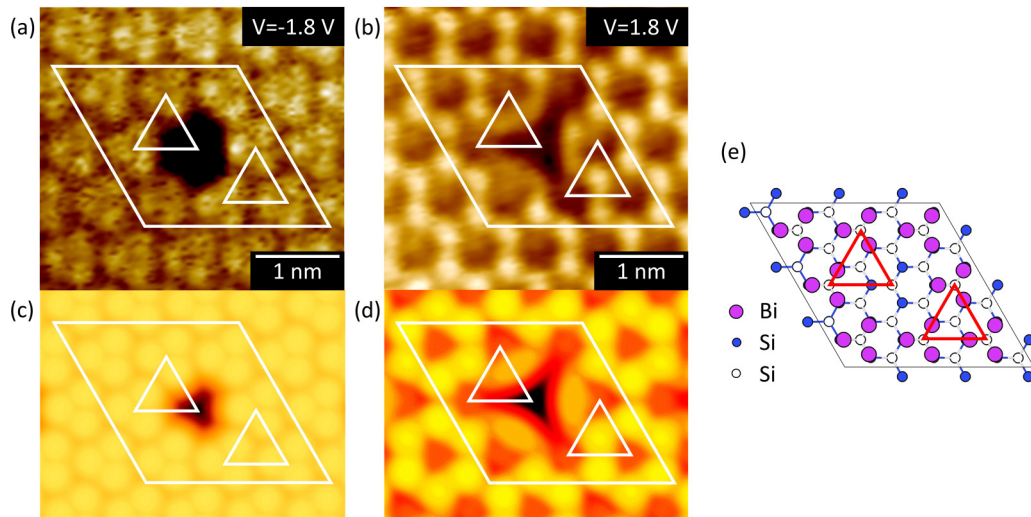


FIG. 4. STM images of a single  $\beta$ -phase vacancy within a  $\beta$ -phase domain at a sample bias of (a)  $-1.8$  V and (b)  $1.8$  V, respectively; (c), (d) DFT simulated STM image at corresponding sample biases; (e) unit cell of the single  $\beta$ -phase vacancy model used for DFT calculation.

reasonable because in this case only two nearest trimers contribute to the Bi in-plane  $p_x, p_y$  states; accordingly, a less intensive and more dispersive pattern is formed. More importantly, the honeycomb center is much brighter than the vacancy center, indicating there are available onsite states above Bi trimers as well. As discussed above, those onsite states originate from overlapped Bi and Si states. From our simulated image in Fig. 4(d), we can easily tell that the  $T_4$  site with three nearest trimers has the highest charge density. Then, the  $T_4$  site with two nearest trimers has a higher charge density than the honeycomb center. Finally, the vacancy center hardly possesses any available states.

The above observations suggest a competition between in-plane Bi  $p_x, p_y$  surface states and out-plane Bi, Si overlapped states, or a competition between offsite honeycomb pattern and onsite hcp pattern. When a  $T_4$  site is surrounded by three nearest Bi trimers, in-plane Bi states play a critical role. A localized bright spot shows up at that site which helps to construct an offsite honeycomb ring. When the  $T_4$  site is surrounded by two nearest trimers, less intensive Bi  $p_x, p_y$  states contribute to a more dispersive offsite pattern and the honeycomb integrity is broken. However, the in-plane states still play a leading role. When there is only one nearest trimer around a  $T_4$  site, such as the single trimer defect discussed in Fig. 3, the out-plane overlapped Bi, Si states take over and onsite hcp pattern shows up in the STM image. It is also critical to mention that in Nagaoka's STS paper the honeycomb pattern was believed to result from underlying  $T_4$ -site Si states rather than Bi surface states, which is not consistent with our  $\beta$ -phase vacancy image here [16]. This is because if that is the case, then the  $\beta$ -phase vacancy should not break the honeycomb integrity at LBES since those  $T_4$  sites are initially adatom-free and introduction of a vacancy should make a trivial change to charge density at those sites.

Finally, we focus on a single  $\alpha$ -phase defect within a  $\beta$ -phase domain as shown in Fig. 5, where 5(a) and 5(b) correspond to a sample bias of  $-1.8$  V (filled state) and  $1.8$  V (LBES), respectively. The filled-state image here is similar to that of  $\beta$ -phase vacancy shown in Fig. 4(a) except that

the center  $\alpha$ -phase Bi adatom can be easily recognized. Also, this single Bi adatom aligns with other  $\beta$ -phase Bi trimers in both lattice vector directions, indicating its  $T_4$ -site adsorption feature. In comparison, LBES image is quite different from that of  $\beta$ -phase vacancy shown in Fig. 4(b). The honeycomb rings are broken near the defect and a forked-road pattern shows up connecting three nearby rings. The structural model for such defect system is plotted in Fig. 5(e) and DFT simulation is established considering Fig. 5(e) as the periodic unit cell, which is also labeled in Figs. 5(a)–5(d). Simulated STM images are shown in Figs. 5(c) and 5(d) in which the center  $\alpha$ -phase dot at filled state and the forked-road pattern at LBES are duplicated. Height difference between the  $\alpha$ - and  $\beta$ -phase in Fig. 5(a) is measured to be  $0.18$  Å, consistent with that in Fig. 3(a). It is confusing that in our simulated STM image [Fig. 5(d)] the Bi defect at LBES is brighter than the honeycomb rings whereas the real STM image [Fig. 5(b)] exhibits the opposite. The discrepancy here might be attributed to the tip-induced band bending at the defect and to the intrinsic error of DFT, which will be further investigated by us in future work. Finally, it should be noted that in comparing Fig. 4 and Fig. 5, it is clear that the defects studied in Ref. [15] are indeed a Bi trimer vacancy, rather than a single  $\alpha$ -phase defect. To investigate the influence of these defects on the surface electronic states, the PDOS for different Bi orbitals have been calculated, as shown in Fig. 6, where 6(a) and 6(b) correspond to the single  $\beta$ -phase defect structure [as shown in Fig. 3(f)] and the single  $\alpha$ -phase defect structure [as shown in Fig. 5(c)], respectively. The orbitals with energies nearest to the Fermi level are shown, which correspond to  $p_x, p_y$  Bi orbitals for the  $\beta$ -phase defect and  $p_z$  orbitals for the  $\alpha$ -phase defect, respectively. Band gaps in both structures are observed to be more or less consistent with that of the defect-free  $\beta$ -phase. For the single  $\beta$ -phase defect structure, the Fermi level shifts towards the valence bands compared to Fig. 2(f), suggesting a holelike feature. Disappearance of Bi  $p_x, p_y$  peaks within the bulk band gap indicates that the single  $\beta$ -phase trimer fails to form surface states. This is consistent with the simulated STM filled-state



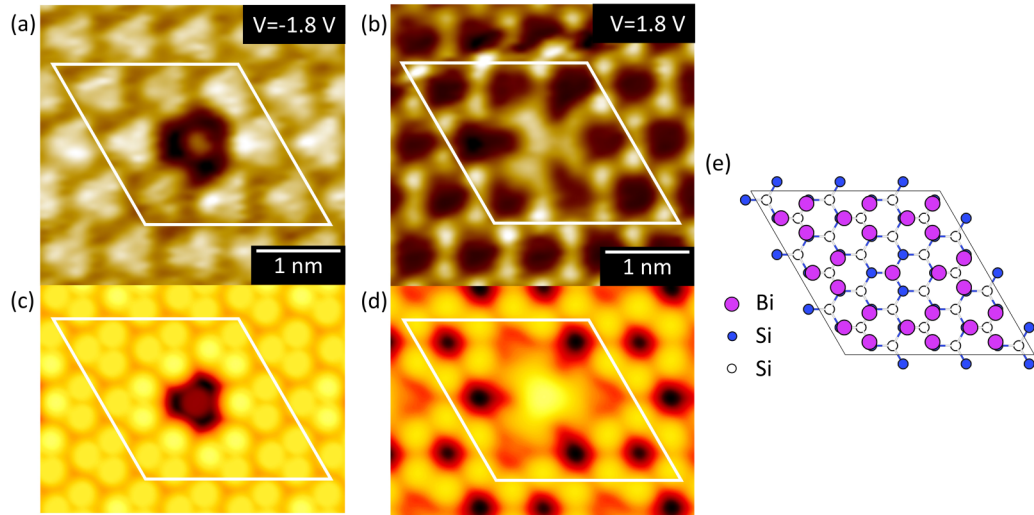


FIG. 5. STM images of a single  $\alpha$ -phase vacancy within a  $\beta$ -phase domain at a sample bias of (a)  $-1.8$  V and (b)  $1.8$  V, respectively; (c), (d) DFT simulated STM image at corresponding sample biases; (e) unit cell of the single  $\alpha$ -phase vacancy model used for DFT calculation.

image [Fig. 3(d)] in which the honeycomb pattern that results from surface states disappears.

For the single  $\alpha$ -phase defect structure, when compared to the PDOS of the pure  $\beta$ -phase surface [Fig. 2(b)], only trivial changes can be observed in the simulated STM image, suggesting the robustness of the  $\beta$ -phase against this type of defect. However, as can be seen in Fig. 6(b), there is a unique peak of the  $\alpha$ -phase Bi  $p_z$  orbital appearing between  $-0.05$  and  $-0.21$  eV, giving rise to a state that is just above what would be the valence-band maximum in the pure  $\beta$ -phase. This state is localized to the  $\alpha$ -phase defect and could be considered to be a quantum dot.

Finally,  $dI/dV$  spectra for single  $\beta$ -phase defect structures and continuous  $\beta$ -phase region are exhibited in Fig. 6(c) in which the black and red curves correspond to the single  $\beta$ -

phase defect and complete  $\beta$ -phase area, respectively. An evident difference between the curves is that a shoulder appears in the complete  $\beta$ -phase spectrum at around  $0.7$  V (empty state). Referring to our DFT calculated PDOS [Fig. 6(b)], this shoulder derives from  $p_x, p_y$  states of Bi trimers. In comparison, the shoulder disappears in the single  $\beta$ -phase defect, supporting our previous interpretation that more than one Bi trimer is required in order to produce surface states.

#### IV. CONCLUSIONS

In conclusion, the Bi on Si(111)  $\sqrt{3} \times \sqrt{3}$   $\beta$ -phase as well as defects in this phase are studied here using STM combined with DFT calculations. First, the bias dependence of STM images combined with both DFT band structure analysis as well as PDOS analysis confirms that the  $\beta$ -phase bias dependence at empty states results from Bi surface states. At low sample bias, Bi  $p_x, p_y$  orbitals result in the offsite honeycomb pattern. At high sample bias, overlapped Si bulk states and Bi surface states give rise to the onsite HCP pattern. Then, by analyzing the single  $\beta$ -phase defect and the  $\beta$ -phase vacancy we further prove that each spot within a honeycomb ring at LBES results from three nearest Bi trimers and missing any of those will break the honeycomb integrity. The single  $\alpha$ -phase defect is also investigated and good agreement is achieved between data and simulations. Finally, our DOS analysis proves that the influence of point defects on  $\alpha$ - and  $\beta$ -phase charge distributions is not significant.

#### ACKNOWLEDGMENTS

This work was funded by Natural Sciences and Engineering Research Council of Canada (NSERC), the Hart Professorship, and the University of Toronto. Computations were conducted on the Niagara homogeneous cluster operated by SciNet and owned by Compute Canada. SciNet is funded by the Canada Foundation for Innovation, NSERC (Grants No. RGPIN-2017-06069 and No. RGPIN-2018-04642), the Government of Ontario, Fed Dev Ontario, and the University of Toronto.

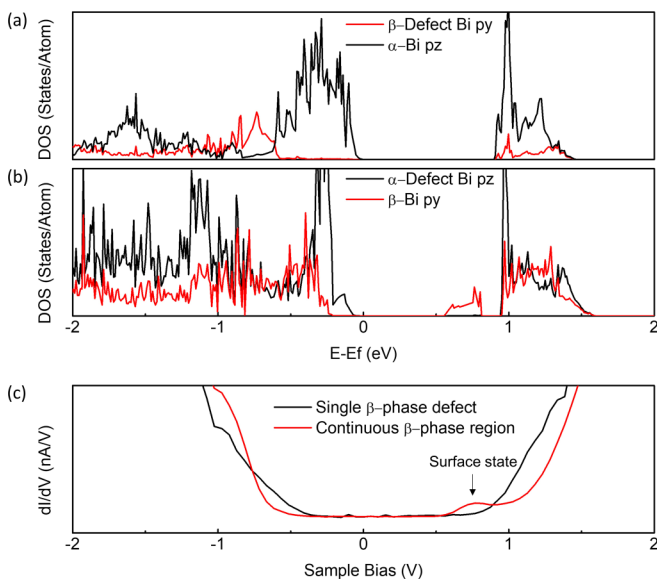


FIG. 6. DFT calculated DOS for (a) single  $\beta$ -phase defect structure and (b) single  $\alpha$ -phase defect structure; (c)  $dI/dV$  spectra for single  $\beta$ -phase defect and continuous  $\beta$ -phase region.

- [1] S.-C. Hsieh, C.-H. Hsu, H.-D. Chen, D.-S. Lin, F.-C. Chuang, and P.-J. Hsu, *Appl. Surf. Sci.* **504** (2020).
- [2] K. Sakamoto, H. Kakuta, K. Sugawara, K. Miyamoto, A. Kimura, T. Kuzumaki, N. Ueno, E. Annese, J. Fujii, A. Kodama *et al.* *Phys. Rev. Lett.* **103**, 156801 (2009).
- [3] A. Takayama, T. Sato, S. Souma, T. Oguchi, and T. Takahashi, *Phys. Rev. Lett.* **114**, 066402 (2015).
- [4] A. Takayama, T. Sato, S. Souma, T. Oguchi, and T. Takahashi, *Nano Lett.* **12**, 1776 (2012).
- [5] F. Reis, G. Li, L. Dudy, M. Bauernfeind, S. Glass, W. Hanke, R. Thomale, J. Schäfer, and R. Claessen, *Science* **357**, 287 (2017).
- [6] C. Park, R. Z. Bakhtizin, T. Hashizume, and T. Sakurai, *Jpn. J. Appl. Phys.* **32**, L290 (1993).
- [7] R. Shioda, A. Kawazu, A. A. Baski, C. F. Quate, and J. Nogami, *Phys. Rev. B* **48**, 4895 (1993).
- [8] K. J. Wan, T. Guo, W. K. Ford, and J. C. Hermanson, *Phys. Rev. B* **44**, 3471 (1991).
- [9] S. Nakatani, T. Takahashi, Y. Kuwahara, and M. Aono, *Phys. Rev. B* **52**, R8711 (1995).
- [10] Y. K. Kim, J. S. Kim, C. C. Hwang, S. P. Shrestha, and C. Y. Park, *Surf. Sci.* **498**, 116 (2002).
- [11] J. M. Roesler, M. T. Sieger, T. Miller, and T. C. Chiang, *Surf. Sci.* **380**, L485 (1997).
- [12] R. H. Miwa, T. M. Schmidt, and G. P. Srivastava, *J. Phys.: Condens. Matter* **15**, 2441 (2003).
- [13] T. Kuzumaki, T. Shirasawa, S. Mizuno, N. Ueno, H. Tochihara, and K. Sakamoto, *Surf. Sci.* **604**, 1044 (2010).
- [14] M. Naitoh, H. Shimaya, N. Oishi, F. Shoji, and S. Nishigaki, *Appl. Surf. Sci.* **123–124**, 171 (1998).
- [15] K. Nagaoka, S. Yaginuma, and T. Nakayama, *Appl. Phys. Lett.* **104**, 111602 (2014).
- [16] K. Nagaoka, S. Yaginuma, and T. Nakayama, *E-j. surf. sci.* **12**, 217 (2014).
- [17] K. Nagaoka, T. Uchihashi, and T. Nakayama, *Surf. Sci.* **644**, 41 (2016).
- [18] J. C. Woicik, G. E. Franklin, C. Liu, R. E. Martinez, I. I. Hwang, M. J. Bedzyk, J. R. Patel, and J. A. Golovchenko, *Phys. Rev. B* **50**, 12246 (1994).
- [19] Y. Haga and K. Takayanagi, *Ultramicroscopy* **45**, 95 (1992).
- [20] G. Kresse and J. Furthmüller, *Phys. Rev. B* **54**, 11169 (1996).
- [21] G. Kresse and D. Joubert, *Phys. Rev. B* **59**, 1758 (1999).
- [22] S. Grimme, *J. Comput. Chem.* **27**, 1787 (2006).
- [23] J. P. Perdew, K. Burke, and M. Ernzerhof, *Phys. Rev. Lett.* **80**, 891 (1998).
- [24] H. J. Monkhorst and J. D. Pack, *Phys. Rev. B* **13**, 5188 (1976).
- [25] J. Tersoff and D. R. Hamann, *Phys. Rev. B* **31**, 805 (1985).
- [26] D. A. Tsukanov, S. G. Azatyan, M. V. Ryzhkova, E. A. Borisenko, O. A. Utas, A. V. Zotov, and A. A. Saranin, *Appl. Surf. Sci.* **476**, 1 (2019).
- [27] J. Gou, L. J. Kong, W. B. Li, S. X. Sheng, H. Li, S. Meng, P. Cheng, K. H. Wu, and L. Chen, *Phys. Chem. Chem. Phys.* **20**, 20188 (2018).
- [28] J. P. Perdew, *Int. J. Quantum Chem.* **28**, 497 (1985).
- [29] R. M. Feenstra and J. A. Stroscio, *J. Vac. Sci. Technol., B: Microelectron. Process. Phenom.* **5**, 923 (1987).